machines

MDPI

Article

Influence of the Two-Stage Femtosecond Laser Processing on AISI 321 Surface Roughness and Optical Parameters

Sergey Dobrotvorskiy [1,2], Yevheniia Basova [1], Borys A. Aleksenko [1], Dmytro Trubin [1], Mikołaj Kościński [2], Paweł Zawadzki [3], Marcel Lojka [4,*] and Michal Hatala [4]

[1] Department of Mechanical Engineering Technology and Metal-Cutting Machines, Institute of Education and Science in Mechanical Engineering and Transport, National Technical University "Kharkiv Polytechnic Institute", Kyrpychova Str. 2, 61002 Kharkiv, Ukraine; sergiy.dobrotvorskyy@khpi.edu.ua (S.D.); yevheniia.basova@khpi.edu.ua (Y.B.); borys.aleksenko@khpi.edu.ua (B.A.A.); dmytro.trubin@mit.khpi.edu.ua (D.T.)

[2] Department of Physics and Biophysics, Faculty of Food Science and Nutrition, Poznan University of Life Sciences, Wojska Polskiego Str. 38/42, 60-637 Poznań, Poland; mikolaj.koscinski@up.poznan.pl

[3] Faculty of Mechanical Engineering, Poznan University of Technology, Plac Marii Skłodowskiej-Curie 5, 60-965 Poznań, Poland; pawel.zawadzki@put.poznan.pl

[4] Faculty of Manufacturing Technologies, Technical University of Košice with a Seat in Prešov, 080 01 Prešov, Slovakia; michal.hatala@tuke.sk

* Correspondence: marcel.lojka@student.tuke.sk

Abstract

The study is devoted to determining the degree of influence of the first and second stages of AISI 321 steel surface treatment with a femtosecond laser, with unchanged laser parameter characteristics, on the blackening parameters and parameters characterizing the distribution of surface heights according to the ISO 25178 standard. Surface blackening is important for production automation for better visibility of markers by optical sensors. The assessment is carried out from the point of view of changing the degree of blackening of the studied surface. During the experiment, it was found that secondary surface treatment without changing the processing mode leads to an insignificant, up to 5%, increase in the degree of surface blackening. Secondary laser processing revealed a diminishing returns effect, where doubling the energy input in perpendicular scanning resulted in only a marginal (~5%) gain in blackening. This phenomenon stems from surface morphological saturation, as the primary roughness parameters *Sq* and *Sdq* attain their plateau values, without contributing to the further formation of hierarchical light-trapping structures. It was also found that during the blackening process, such parameters as the maximum peak height *Sp*, the ten-point surface height *S10z*, and the asymmetry *Ssk* increased more than others. After repeated treatment, the values of the parameters maximum valley depth *Sv* and the root mean square slope *Sdq* increased the most. At the same time, the nature of the normal Gaussian surface height distribution was preserved. As the *Sdq* value increases, the number of randomly located reflecting surfaces increases, and this leads to better scattering of the directed beam. On the other hand, the absence of random fragments on the vertices of the periodic surface structure, which corresponds to a high *Sku* index, allows such a surface to scatter light more effectively.

Keywords: femtosecond laser; secondary processing; automation; markers visibility; blackening

Check for updates

Academic Editor: Kai Cheng

Received: 20 March 2026
Revised: 24 April 2026
Accepted: 27 April 2026
Published: 30 April 2026

Copyright: © 2026 by the authors. Licensee MDPI, Basel, Switzerland. This article is an open access article distributed under the terms and conditions of the Creative Commons Attribution (CC BY) license.

1. Introduction

In modern mechanical engineering, there is always a need to use improved methods and additions to existing surface machining processes [1]. Powerful, efficient, and flexible laser processing technology is the most promising direction for improving the surface finishing process [2]. The transition from contact sensors, detectors, and limit switches to contactless optical sensors requires increased attention to ensuring the conditions for their reliable operation. The operation of sensors in lighting conditions, in the presence of glare and flares, requires obtaining special marking surfaces that absorb light well to ensure better contrast, information content, and readability of information by optical sensors. Laser treatment is well-suited for this purpose. For example, femtosecond lasers can be used to make surface blackening, wettability and create surface microstructures with unique optical and sliding properties [3,4]. Laser irradiation makes it possible to create complex two-level microstructures [5] that have roughness properties at the macroscopic and microscopic levels [6]. The structures obtained as a result of laser processing can be periodic [7] and formed either by controlled action or obtained in parallel with imparting other specified properties to the surface [8,9]. In modern industry, the fabrication of functional surfaces with nanometer precision is achieved through various techniques, with ultra-precision machining traditionally being prominent. Research into material removal mechanisms at the nanoscale and subsurface damage formation, including studies utilizing molecular dynamics (MD) simulations [10], demonstrates the inherent complexity of achieving defect-free surfaces. To overcome the limitations of mechanical cutting, such as tool wear and microcrack formation in brittle materials, hybrid methods involving laser-assisted and vibration-assisted machining [11,12] have been actively developed. While the development of innovative multi-axis nano-machining devices enables the creation of hierarchical structures [13], direct femtosecond laser treatment remains a unique non-contact method for rapidly modifying the optical properties of metals without the need for complex mechanical tooling. The effect of the laser processing method cannot be achieved by mechanical processing, such as cutting and grinding [14]. The properties of the processed surface are assessed based on modern standards. The international standard ISO25178 offers dozens of parameters for determining the microstructure of the studied surface [15]. Determining the pattern of changes in roughness parameters in the process of imparting the required surface properties improves the quality of production and control in the process of technical processing, helps to accelerate and simplify the implementation of these processes, and expands the scope of practical application of modern mechanical engineering standards. A practical study carried out to determine the effect of surface re-processing based on parameters characterizing the surface height distribution allows us to draw conclusions about the feasibility of re-processing for solving specific problems [16,17] of laser surface processing.

With the increasing role of standardization in modern mechanical engineering, the assessment of surface roughness parameters [18] from the point of view of the ISO 25178 standard plays an important role. The real surface geometry is so complicated that a finite number of parameters cannot provide a full description [19].

Standard ISO 25178 is a widely recognized reference framework of indices and procedures, which can help accelerate understanding of functional information. Such indices have been developed specifically for the micro-scale [20]; however, they can also be successfully implemented in the case of larger scales [21]. The standard defines material measures for the calibration of 2D-topography [22] and 3D-topography measurement devices [23]. Some of the suggested material measures have been established within the industrial application for a long time, while others [24] have not yet been extensively researched regarding their practical abilities [25]. Areal 3D analysis of surface texture gives more opportunities than a study of 2D profiles. Surface topography evaluation, considered as a 3D dimensional

analysis [26] in micro or nanoscales, plays an important role in many fields of science and life [27,28]. Among many texture parameters [29], those connected with height are the most often used. However, there are many other parameters and functions that can provide additional important information regarding the functional behavior of surfaces [30,31] in different applications [32,33]. The mechanism driving the appearance change in the surface texture, topography, and roughness [34,35] of the treated samples has been studied by many researchers. The results indicate that the size and shape of laser processing-induced microscale cavities on the surface [36] may account for the differences in the samples' appearance [2]. We study the correlation of the properties of surfaces processed with a femtosecond laser [37,38] with the values of the standard ISO 25178 parameters.

Recent advances in ultrafast laser surface functionalization have demonstrated the potential for precise control over material properties through the formation of Laser-Induced Periodic Surface Structures (LIPSS) [39,40]. These sub-wavelength structures can significantly modify the optical and wetting characteristics of austenitic stainless steels. However, achieving specific industrial goals, such as maximum blackening or superhydrophobicity, often requires multi-objective optimization strategies to balance surface roughness, processing speed, and chemical stability. While much research has focused on the low-fluence regime for regular nano-structuring, the transition to high-fluence, multi-stage processing remains a critical area for developing durable, high-contrast markers suitable for automated sensing environments. This study builds upon these developments by investigating the saturation limits of hierarchical structures formed under intensive ablation regimes.

Recent studies, synthesized in a comprehensive review [41], highlight the role of periodic structures in surface engineering. Parallel to this, researchers have focused on multi-objective optimization to balance processing speed and optical performance, demonstrating that for austenitic steels, the transition from regular nanostructures to hierarchical micro-voids requires precise parameter control to avoid energy inefficiency.

2. Materials and Methods

Plates made of AISI 321 steel were processed using a high-power femtosecond fiber laser system, Jasper X0-20 (FLUENCE Technology, Warszawa, Poland). The choice of AISI 321 austenitic stainless steel as the substrate is dictated by its widespread application in critical industries, such as aerospace, nuclear, and chemical engineering, where components often operate under high temperatures and in corrosive environments. In such conditions, conventional marking methods (e.g., ink or chemical etching) are prone to degradation. Therefore, developing high-contrast, permanent laser-induced markers on this specific steel grade is essential for reliable automated tracking and sensor-based identification in harsh industrial settings. Furthermore, the presence of titanium as a stabilizing element in AISI 321 adds a unique metallurgical dimension to the study of laser-matter interaction and subsequent oxide layer formation. The sample dimensions were 0.035 m $\times$ 0.07 m $\times$ 0.0015 m. The laser radiation was delivered to the treated surface through a galvanometric scanning head. The main laser processing parameters used in the experiments are presented in Table 1.

The laser operated with linear polarization, controlled by a half-wave plate. The pulse duration was less than 250 fs. Surface microrelief analysis was performed with the aid of a ZEISS AXIO HAL 100 optical microscope (Figure 1, Carl Zeiss AG, Jena, Germany). Surface cross-sections were obtained using an Alicona IF-Portable RL optical microscope (Bruker Alicona, Graz, Austria).

To ensure the reproducibility of the results, surface topography measurements were performed in at least three independent regions for each sample. The obtained data were averaged, and the standard deviation was calculated to demonstrate statistical significance. The surface microrelief analysis was conducted using an Alicona IF-Portable RL system with

a vertical resolution of 10 nm and a lateral resolution of 0.5 µm. Prior to the experimental series, the profilometer was calibrated using a certified step-height standard. Optical characterization was performed with a ZEISS AXIO HAL 100 microscope (Carl Zeiss AG, Jena, Germany), calibrated with a standard stage micrometer (10 µm division). The measurement uncertainty for the reported S-parameters was estimated to be within 1.0%.

Table 1. Laser parameters.

Parameter	Dimension	Value
Peak fluence	J/cm^2	20
Spot size	µm	25 ± 0.5
Focal spot area	m^2	8×10^{-11}
Pulse frequency	MHz	2
Single pulse energy	µJ	50
Wavelength	nm	1030
Pulse duration	fs	<250
Beam quality	M^2	<1.3
Average power	W	100

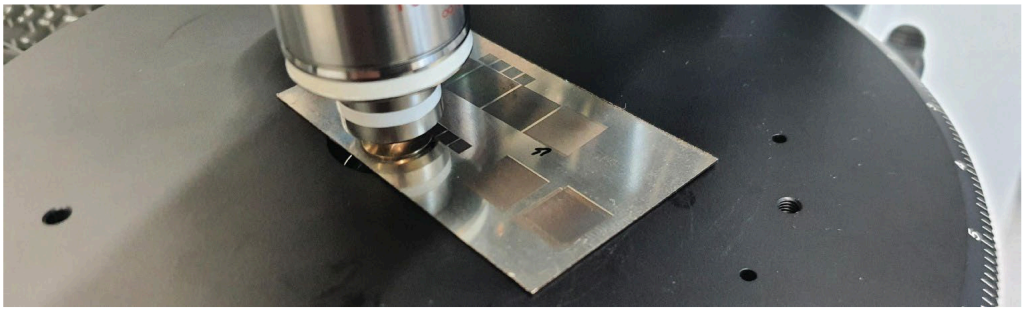


Figure 1. The studied plate on the Microscope AXIO HAL 100.

The properties of the first sample were studied after a single laser treatment of its surface (Figure 2A, item 1). The surface of the second sample was processed in two stages. After an initial treatment similar to that of the first sample (Figure 2B, item 1), the surface was secondary processed (Figure 2B, item 2), resulting in an overlap zone of two sections of successive processing steps (Figure 2B, item 3), where the surface was successively subjected to double laser irradiation. The scanning direction during secondary processing was perpendicular to the primary scanning direction. The rest of the laser processing parameters and energy values remained unchanged. The experiment yielded surfaces characterized by varying roughness profiles and distinct visual gradients of blackness (Figure 2A, item 1, Figure 2B, item 3).

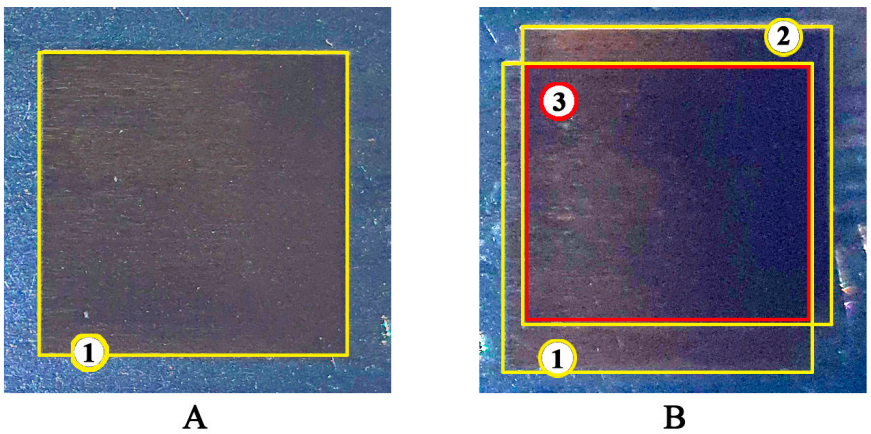


Figure 2. *Cont.*

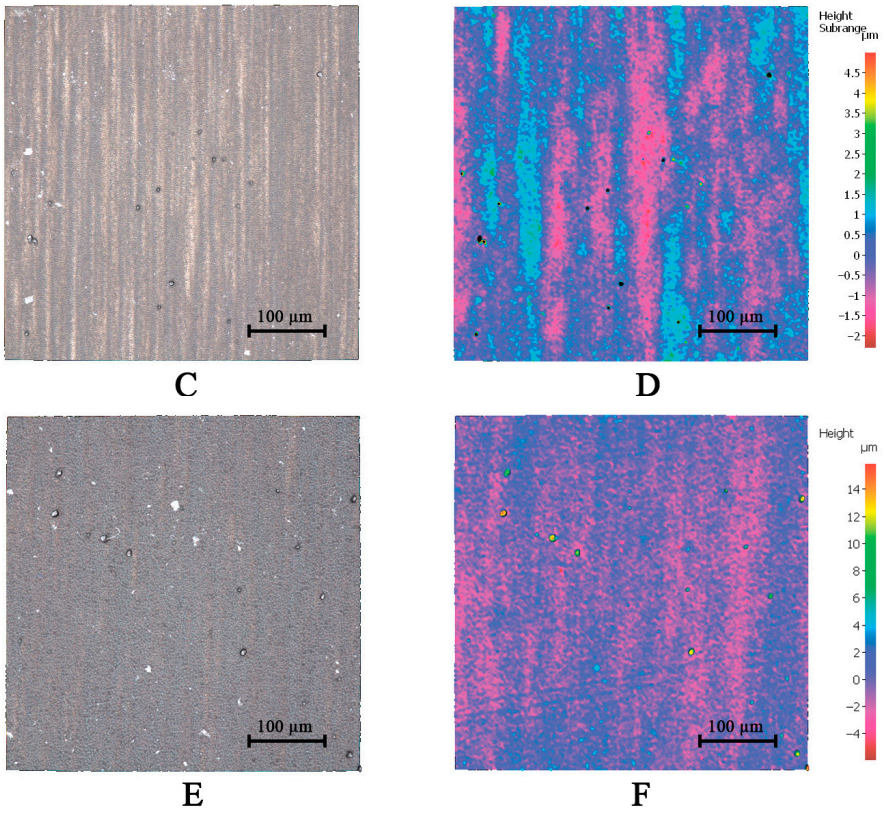


Figure 2. AISI 321 steel surface view after primary and secondary processing. (**A**)—surface AISI 321, primary processing; (**B**)—surface AISI 321, secondary processing; the numbered boxes indicate the different processing stages: 1 (yellow box)—area after primary processing; 2 (yellow box)—area after secondary processing; 3 (red box)—the overlapping region that underwent both primary and secondary processing; (**C**)—surface primary processing, view through a ZEISS AXIO optical digital microscope (Carl Zeiss AG, Jena, Germany); (**D**)—primary processing, Surface Height gradient, ZEISS AXIO microscope; (**E**)—surface secondary processing, view through a ZEISS AXIO optical digital microscope; (**F**)—secondary processing, Surface Height gradient, ZEISS AXIO microscope (Carl Zeiss AG, Jena, Germany).

The software used to process data obtained during microscopy is supplied with the equipment used and is therefore completely compatible with it.

When studying the properties of the surfaces studied, determining (*Smr1*, *Smr2*), asymmetry (Skewness) *Ssk*, kurtosis (Kurtosis), (*Sku*), and other indicators, technologies for assessing the surface microrelief are used in accordance with ISO 25178.

To characterize the surface properties, areal topography parameters, including material ratios (*Smr1*, *Smr2*), skewness *Ssk*, and kurtosis (*Sku*), were evaluated in accordance with the ISO 25178 standard:

$$Ssk = \frac{1}{Sq^3} \iint\limits_A (z(x,y))^3 dxdy \quad (1)$$

$$Sku = \frac{1}{Sq^4} \iint\limits_A (z(x,y))^4 dxdy \quad (2)$$

where

$$Sq = \sqrt{\frac{1}{A} \iint\limits_A (z(x,y))^2 dxdy} \quad (3)$$

$$S10z = S5q + S5v \quad (4)$$

$$Sdq = \sqrt{\frac{1}{A}\iint_A \left(\left(\frac{\partial z(x,y)}{\partial x}\right) + \left(\frac{\partial z(x,y)}{\partial y}\right)\right)^2 dxdy} \quad (5)$$

The material portions of the peaks (*Smr1*) and the deeper valleys (*Smr2*), along with the reduced peak height (*Spk*) and reduced valley depth (*Svk*), were derived from the areal material ratio curve (Firestone-Abbott curve) using the microscope's integrated software. The degree of blackening of the samples was assessed visually and in a graphical editor using color data in the HSB value range.

Verification of the spot size involved measuring the ablation zone widths on a Jeol 7001TTLS scanning electron microscope (SEM) at minimal pulse energies close to the ablation threshold, resulting in a value of 25 μm.

According to literature data for AISI 321 steel [42,43], the ablation threshold *Fth* for femtosecond pulses is approximately $0.1-0.2$ J/cm^2, corresponding to an optimal fluence for clean ablation of $F_{opt} \approx 0.7-1.5$ J/cm^2. In our study, a significantly higher fluence of $F_0 > 20$ J/cm^2 was employed, which is 15–20 times greater than F_{opt}. This high-energy regime was chosen intentionally to ensure deep texturing and the formation of chaotic structures necessary for surface blackening. Consequently, the absence of minimal roughness in our results is entirely consistent with the theory, as the process occurs in an intensive ablation mode aimed at achieving maximum optical absorption rather than surface finishing or polishing. The use of a high overlap ratio (>95%) was an intentional choice. This facilitated a heat accumulation effect and enabled multiple exposures to the same zone, which is critical for the deep transformation of the micro-relief and for achieving maximum light absorption.

3. Results and Discussion

Visually, when assessing enlarged images of the surfaces of AISI 321 primary processing (Figure 2C) and AISI 321 secondary processing (Figure 2E), there are no indications that ordered periodic structures were formed (Figure 2C,E). Surface height profiles captured both longitudinal (Figures 3 and 4) and transverse (Figures 5 and 6) of the laser scanning path further demonstrate the stochastic microstructure of the AISI 321 surfaces following primary and secondary processing.

The cross-sectional height curves of the surfaces (Figure 2C,E) indicate the chaotic nature and lack of periodicity of the microstructure of the surfaces of AISI 321 primary processing and AISI 321 secondary processing, resulting in comparable color signatures (Figure 2A,B), despite the difference in the number of surface treatment processes performed on samples.

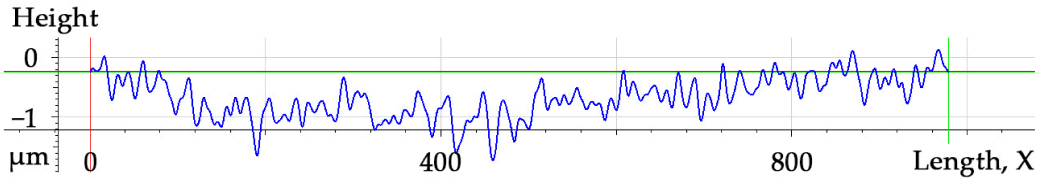


Figure 3. AISI 321 primary processing. X-coordinate cross-sectional curve. The red and green crosshairs denote the start and end points of the measured profile path, respectively.

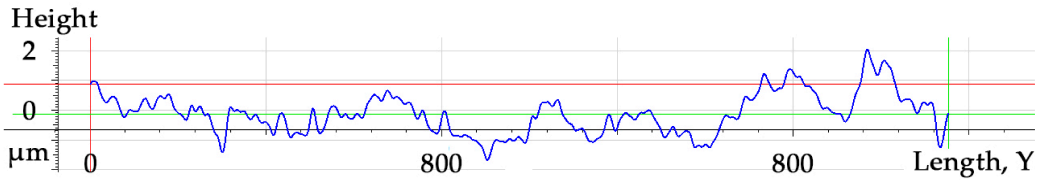


Figure 4. AISI 321 primary processing. Y-coordinate cross-sectional curve. The red and green crosshairs denote the start and end points of the measured profile path, respectively.

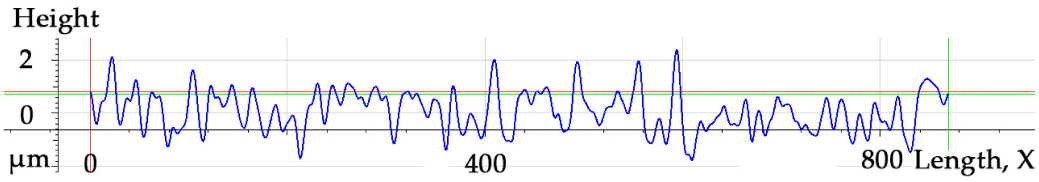


Figure 5. AISI 321 secondary processing. X-coordinate cross-sectional curve. The red and green crosshairs denote the start and end points of the measured profile path, respectively.

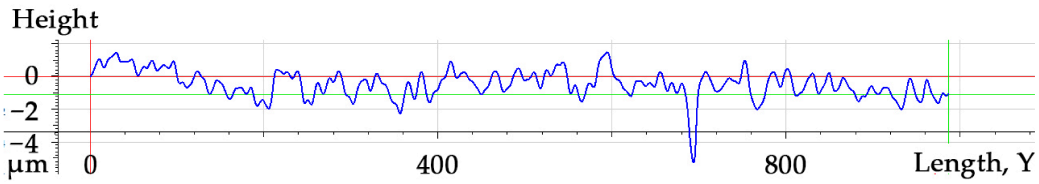


Figure 6. AISI 321 secondary processing. Y-coordinate cross-sectional curve. The red and green crosshairs denote the start and end points of the measured profile path, respectively.

For objective verification of the results, the surface of the studied samples was divided into 10 regions, from 1.0 to 1.9 for the first sample and from 2.0 to 2.9 for the second sample (see Figure 7). Data on the blackness in each region of both samples were obtained and the average values of blackness for the two samples were calculated.

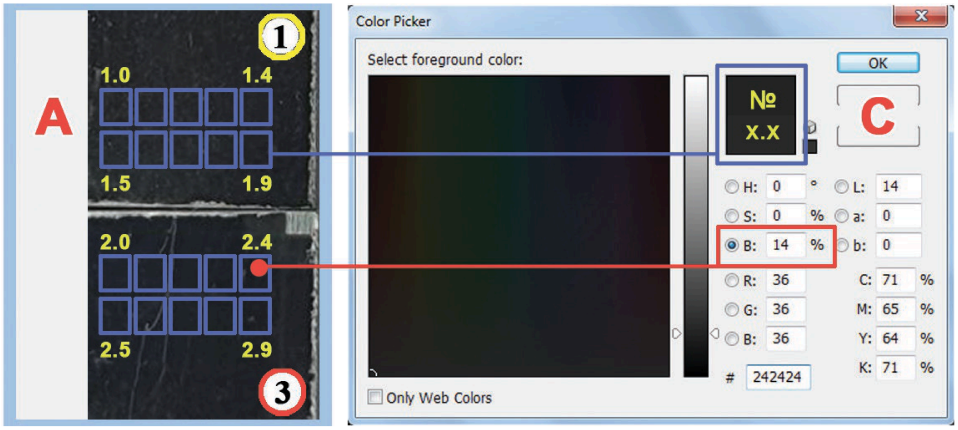


Figure 7. Obtaining data on the blackness of the studied samples using a graphical editor. A—photo of samples: 1—primary processing surface; 3—secondary processing surface. C—determination of darkness ([B] in the range of HSB values) using a graphic editor.

To ensure maximum data fidelity and eliminate the influence of imaging conditions, such as light intensity, glare, and exposure, all investigated areas were photographed simultaneously in a single frame under diffused lighting. The subsequent segmentation of the image into individual zones was performed solely for the convenience of presentation in the manuscript. Thus, any recorded differences in HSB values are strictly attributable to the properties of the surface itself rather than the data acquisition conditions.

The averaged data for the analyzed specimens are summarized in Table 2. Since the applied method quantifies surface brightness, the values decrease as the surface darkens, reaching 0% for an ideal black body (perfectly black surface).

Table 2. Blackening data for primary processing surface and secondary processing surface.

Degree of Blackening %	1	2	3	4	5	6	7	8	9	10	Average	Standard Deviation
Primary processing	16	17	16	17	18	16	16	16	17	17	16.6	0.699206
Secondary processing	14	14	15	14	14	16	14	15	14	14	14.4	0.699206

The obtained data indicate a slight, within 2 percent (Table 2), blackening of the surface after secondary processing. Thus, additional post-processing of the surface without changing the processing mode does not lead to a twofold increase in the degree of surface blackening compared to the nature of the surface blackening obtained as a result of the previous processing. Statistical analysis of the brightness (HSB) data revealed remarkable consistency in the measurement system. Despite the differences in mean blackening levels (16.6% and 14.4%), the standard deviation in both cases was an identical 0.7. Additionally, statistical significance was confirmed by a two-tailed Welch's *t*-test. The obtained *p*-value ($p < 0.001$) confirms that the instrumental error level remains constant throughout the digital image analysis, indirectly supporting the high reliability of the observed 5% increase in the Blackening value.

The comparative analysis of the surface truncation coefficients for a scale-limited area (Figure 8) was performed by superimposing the material ratio (Firestone-Abbott) curves (Figure 9) of the primary processing surface (blue line) and the graph of the Firestone-Abbott curve (Figure 10) of the secondary processing surface (pink line); a divergence of the curves is noticeable (shown by arrows).

Specifically, in the peak zone (left side of the graph), the secondary processing curve shifts upward, reflecting a nearly twofold increase in the reduced peak height (*Spk*) from 0.686 µm to 1.400 µm. Conversely, in the valley zone (right side of the graph), the curve shifts downward, indicating an increase in the reduced valley depth (*Svk*) from 0.539 µm to 1.030 µm (Table 3).

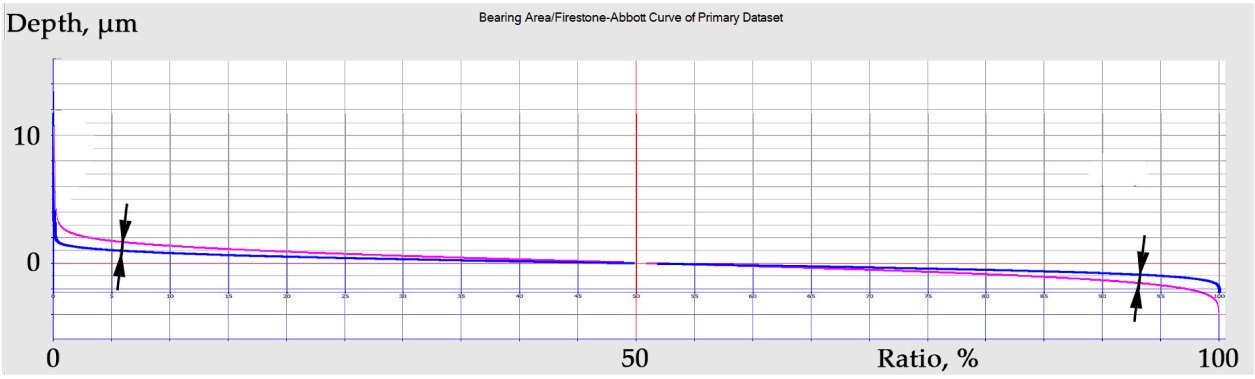


Figure 8. Comparative graph of the curves for the values of the crumpling coefficient of the scale-limited surface area (Abbott-Firestone curves) of the AISI 321 primary processing and AISI 321 secondary processing samples: the blue line represents primary processing, while the pink line represents secondary processing. The arrows indicate the divergence of the curves.

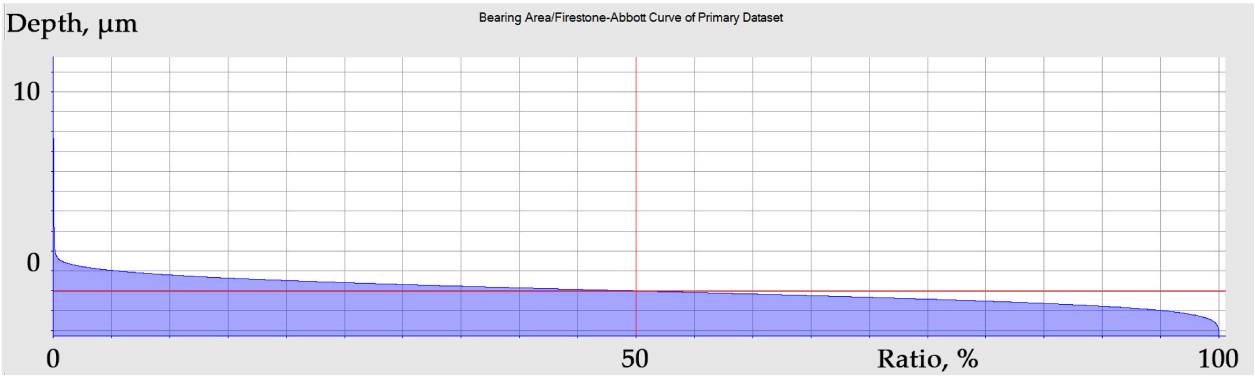


Figure 9. AISI 321 primary processing. Graph of the curve for the crumpling coefficient of a surface area of a limited scale (Abbott-Firestone curve).

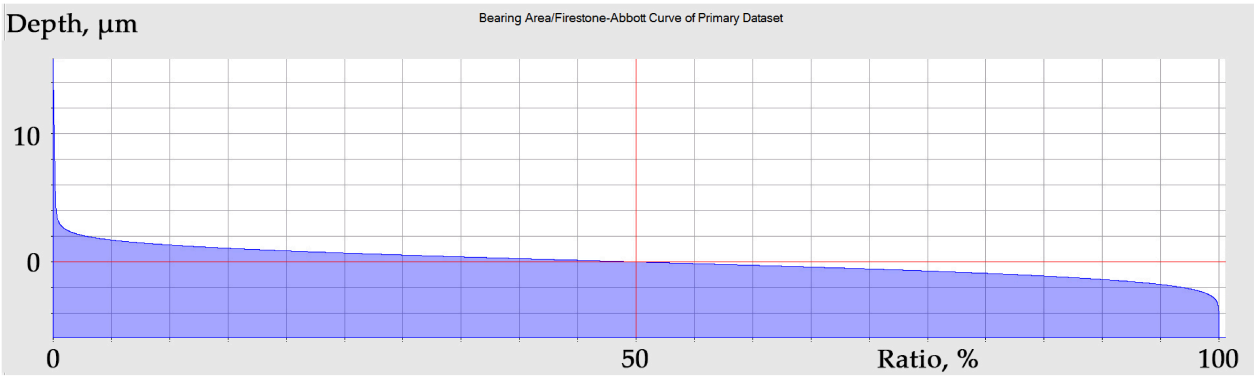


Figure 10. AISI 321 secondary processing. Graph of the curve for the crumpling coefficient of a surface area of a limited scale (Abbott-Firestone curve).

Table 3. Surface topography parameters of the AISI 321 specimens in accordance with ISO 25178, obtained using an Alicona IF-Portable RL optical microscope. ΔI = PP/B—ratio of the parameter value of the primary processing surface to the base surface; ΔII = SP/B—ratio of the parameter value of the secondary processing surface to the base surface; ΔIII = SP/PP—ratio of the parameter value of the secondary processing surface to the primary processing surface.

Param.	Dim.	Base	AISI 321 Primary Processing	AISI 321 Secondary Processing	ΔI = PP/B	ΔII = SP/B	ΔIII = SP/PP
Sk	µm	-	1.615	2.717	-	-	1.68
Spk	µm	-	0.686	1.400	-	-	2.04
Svk	µm	-	0.539	1.030	-	-	1.91
Smr1	%	-	9.990	9.490	-	-	0.94
Smr2	%	-	91.110	89.840	-	-	0.98
Vmp	mL/m^2	-	0.034	0.069	-	-	2.02
Vmc	mL/m^2	-	0.556	0.950	-	-	1.71
Vvc	mL/m^2	-	0.762	1.265	-	-	1.66
Vvv	mL/m^2	-	0.065	0.122	-	-	1.88
Vvc/Vmc	-	-	1.372	1.332	-	-	0.97
Sa	µm	0.191	0.497	0.855	2.60	4.48	1.72
Sq	µm	0.242	0.646	1.155	2.67	4.77	1.79
Sp	µm	1.598	11.716	15.820	7.33	9.90	1.35
Sv	µm	1.103	2.297	5.914	2.08	5.36	2.57
Sz	µm	2.701	13.995	21.735	5.18	8.05	1.55
S10z	µm	1.853	11.194	19.712	6.04	10.64	1.76
Ssk	-	−0.146	1.210	1.585	−8.29	−10.86	1.31
Sku	-	3.593	17.505	19.107	4.87	5.32	1.09
Sdq	-	0.037	0.133	0.315	3.60	8.51	2.37

A more prominent microstructure (Figures 10 and 11) of the surface of AISI 321 secondary processing (Figure 2A) compared to the microstructure (Figures 12 and 13) of AISI 321 primary processing (Figure 2B) indicates a significant deviation of the curve from the mean profile height (*Rk*). The core roughness height parameter (*Sk*) of the AISI 321 secondary processing curve is 2.717 µm (Table 3), which is more than one and a half times greater than the value of the parameter (*Sk*) of the AISI 321 primary processing surface curve, which is 1.615 µm (Table 3). This indicates that repeated processing increases the relief of the surface microstructure.

This simultaneous expansion of the curve in both peak and valley regions, combined with the steepening of the core slope (*Sk*), provides a comprehensive quantitative confirmation that secondary laser processing amplifies the vertical amplitude of the micro-relief, creating a more pronounced hierarchical structure.

The values of the reduced peak height (*Spk*) = 1.400 µm and reduced valley depth (*Svk*) = 1.030 µm parameters of the AISI 321 secondary processing surface are twice as large as the values of the corresponding parameters of the AISI 321 primary processing surface, (*Spk*) = 0.686 µm and (*Svk*) = 0.539 µm (Table 3). Thus, repeated processing doubled

the surface relief. A more prominent microstructure, according to visual assessment, also contributes to the blackening of the surface, although, as noted earlier, a multiple increase in values does not lead to a corresponding increase in the level of blackening.

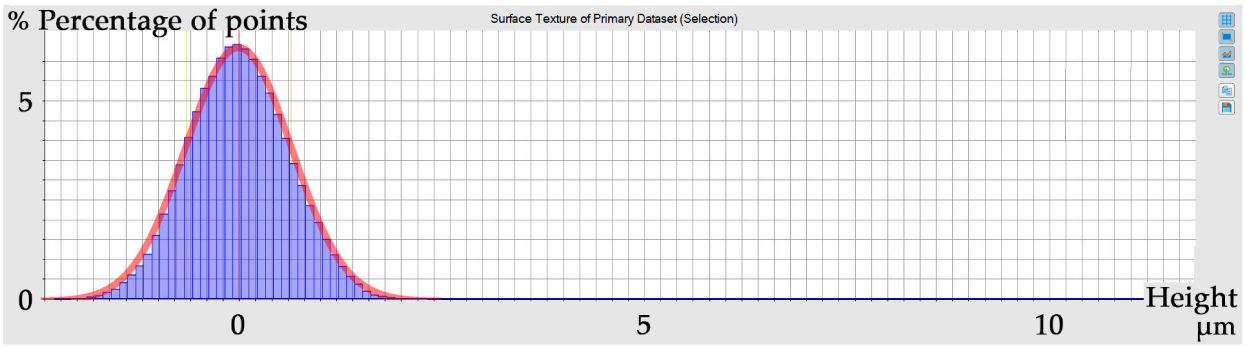


Figure 11. AISI 321 primary processing. Surface height distribution diagram.

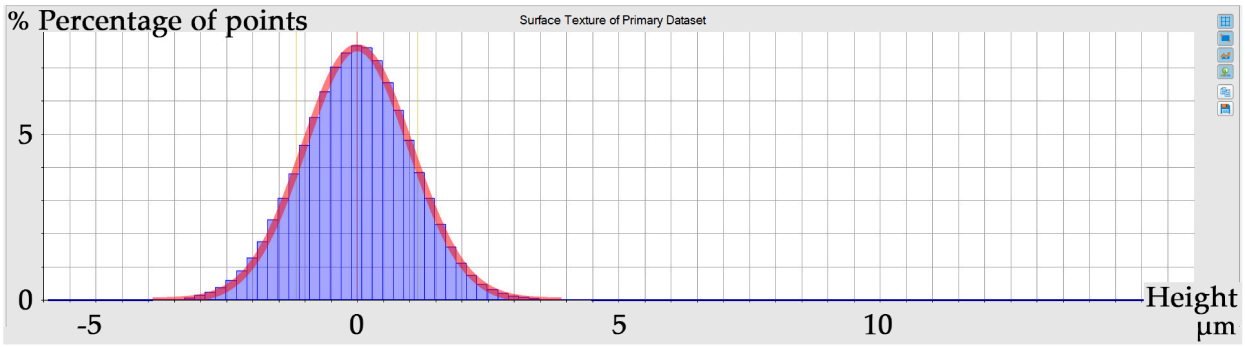


Figure 12. AISI 321 secondary processing. Surface height distribution diagram.

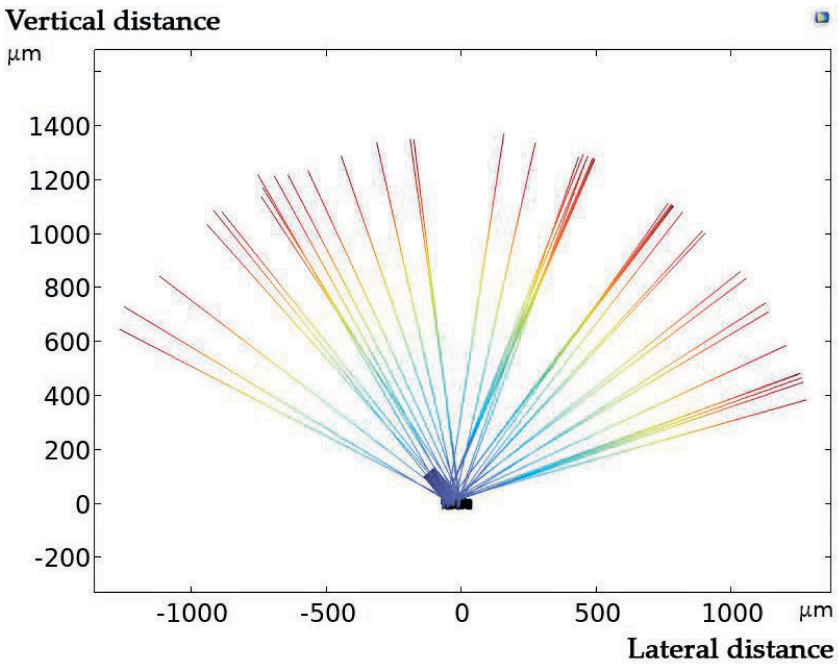


Figure 13. Reflectivity diagram from a surface with a low kurtosis index, *Sku*.

It is observed that the peak material portion (*Smr1*) and the valley material portion (*Smr2*) exhibit no substantial deviation between the two compared surfaces: AISI 321 primary processing (*Smr1*) = 9.990%, (*Smr2*) = 91.110%; AISI 321 secondary processing

(*Smr1*) = 9.490%, (*Smr2*) = 89.840% (Table 3). From this, we can conclude that repeated laser processing does not reduce the proportion of the surface that can be removed during the lapping (Peak material portion) (*Smr1*). Likewise, the proportion of hollows on the surface that serve to accumulate additives and lubricating coatings on the surface of the sample does not change noticeably. Thus, for a qualitative change in the surface optical properties, processing with modified laser parameters is required, but not multiple sequential processing in a fixed mode.

The ratio of parameters (*Smr1* and *Smr2*) before and after repeated laser processing also suggests that the prevalence of peaks and valleys on the surface of the material (as well as their deficiency) is not decisive for the level of surface blackening, since the degree of darkness changed after the second treatment process within 2.5% (Table 2).

When characterizing the surfaces based on the height distribution parameters (*Ssk*), close, within the experimental error, values of the profile asymmetry parameter (*Ssk*) = 1.210 of the AISI 321 primary processing surface (Figure 2A) and the values of this parameter (*Ssk*) = 1.585 for the AISI 321 secondary processing surface (Figure 2B) are noted (Table 3). The surface morphology is characterized by a preponderance of peaks relative to the volume of valleys and recessed features. Thus, this feature of the microrelief is preserved after repeated processing.

Also, for the surfaces under consideration, a high value of the peak coefficient parameter is observed: (*Sku*) = 17.505 for the surface of AISI 321 primary processing (Figure 2A), and (*Sku*) = 19.107 for the surface of AISI 321 secondary processing (Figure 3 and Table 3). An increase in kurtosis (*Sku*) is shown to correlate with surface darkening; yet a minor discrepancy within 5% in this topographic metric does not yield a significant visual contrast between the compared specimens (Figure 2A,B).

The height distribution profiles for the studied surfaces exhibit a significant morphological similarity, particularly in the case of the primary laser-processed AISI 321 (Figure 2A) and the primary secondary laser-processed AISI 321 (Figure 2B). The diagrams indicate that the distribution of heights has a Gaussian distribution (Figures 11 and 12.). For clarity, in the figures (Figures 11 and 12), the Gaussian nature of the distribution is shown by an additional red curve.

It can be stated that if, during the initial processing, a periodic surface microstructure is not formed and a complex height distribution is not observed, then repeated surface treatment in the same mode does not impart a periodic character to the surface structure and does not change the nature of the height distribution (Figures 11 and 12).

Computer models, built in the COMSOL® v. 6.2 Multiphysics environment using the Ray Optics module [44], of the reflection of a narrow beam of light from a surface with a low flatness index (*Sku*) (Figure 13) and a high flatness index (*Sku*) (Figure 14) indicate better scattering of the beam by the scattering surface with an increase in this index. The reflection coefficient in the model calculation is set at 0.3. The reason for the worse scattering is the apical fragments of the microstructure (Figure 15, pos. a), which effectively reflect the beam of light (Figure 15). The absence of such reflecting surfaces in a microstructure with a high index (*Sku*) allows such a surface to scatter light more effectively (Figure 16).

Computer models of the reflection of a narrow beam of light from a surface with a low value of local gradients (*Sdq*) (Figure 17) and a high value of local gradients (*Sdq*) (Figure 18) also indicate better scattering of the beam by the scattering surface with an increase in this value. The reason for the worse scattering with a low (*Sdq*) is the absence of a large number of reflecting surfaces on the surface, randomly located at different angles relative to the direction of incidence of the beam (Figure 19). As the (*Sdq*) value increases, the number of randomly positioned reflecting surfaces increases, which leads to better scattering of the directed beam (Figure 20).

The increase in the Sdq parameter (root-mean-square slope) from 0.133 to 0.315 serves as a key indicator of the surface topographic evolution. From the perspective of radiation-matter interaction, the increase in local relief gradients initiates a multiple reflection mechanism within the micro-cavities. Each incident photon striking a steep asperity slope (indicated by the high Sdq) is not reflected into the hemisphere but is redirected deeper into the structure. According to the Bouguer–Lambert–Beer law and the geometric trap principle, the total absorption increases proportionally to the number of interaction acts $(1 - \boldsymbol{R})^{\boldsymbol{n}}$, where n is the number of reflections. Thus, the observed secondary blackening is attributed not only to the growth in roughness amplitude but also to the effective energy redistribution within hierarchical irregularities, which transform the surface into a highly efficient optical trap.

This mechanism is confirmed by the results of modeling in the COMSOL Multiphysics environment (Figures 13–20), which clearly demonstrate an increase in the capture of rays with an increase in the steepness of the microrelief.

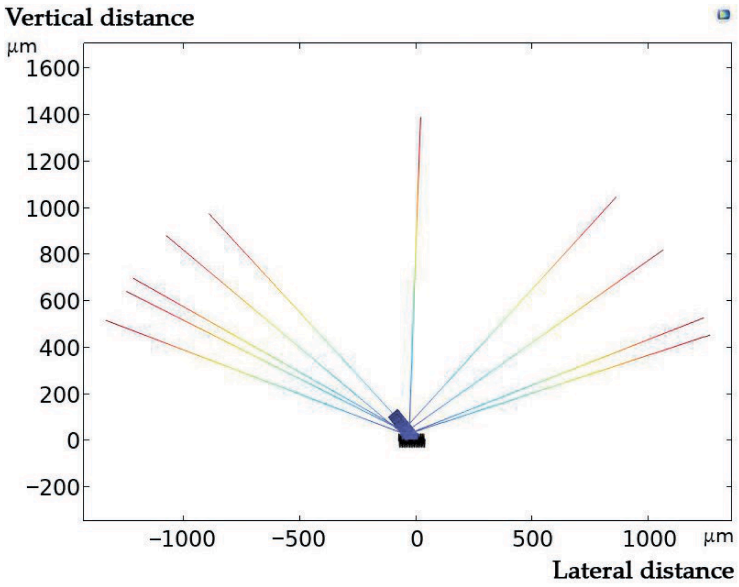


Figure 14. Reflectivity diagram from a surface with a high kurtosis index, *Sku*.

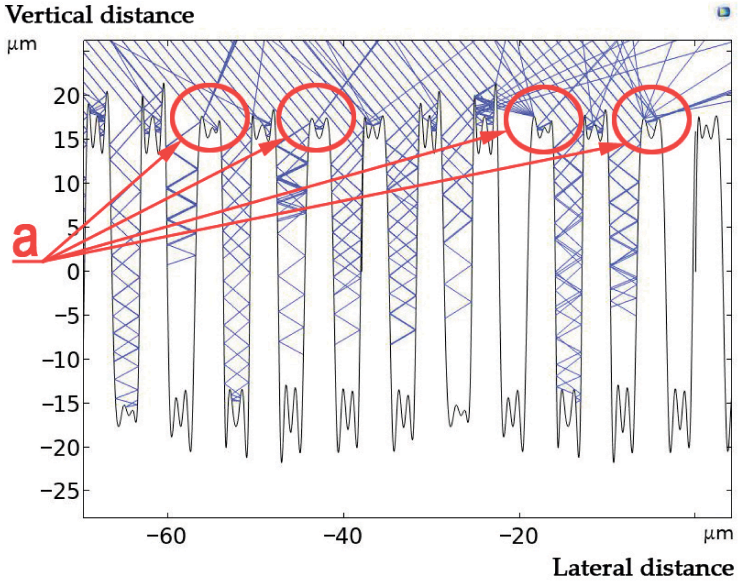


Figure 15. Light beam propagation diagram in a microstructure with a low flatness index, *Sku*; a—reflection of rays from the peaks of surface structural elements.

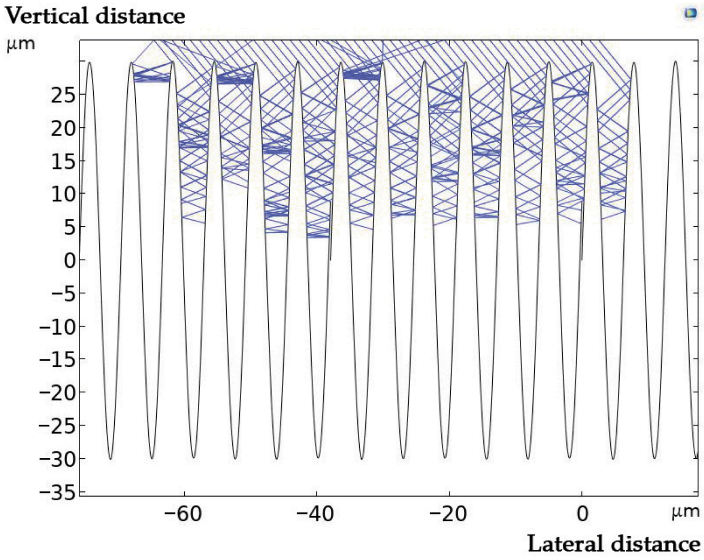


Figure 16. Light beam propagation diagram in a microstructure with a high flatness index, *Sku*.

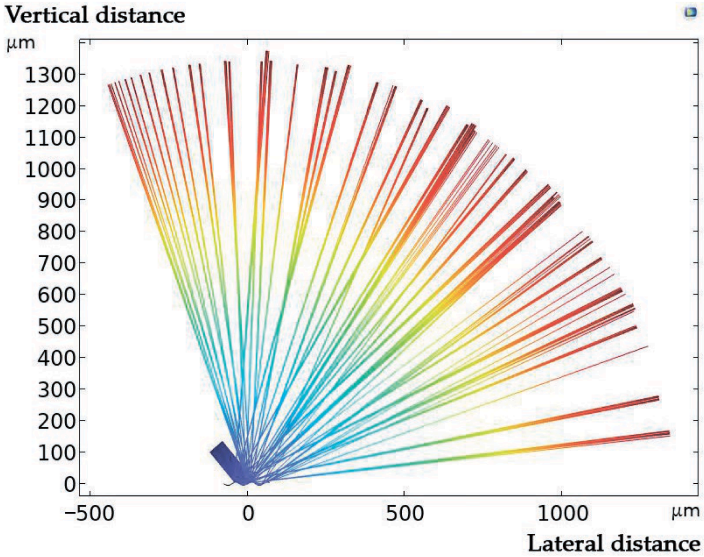


Figure 17. Reflectance diagram from a surface with a low value of local gradient *Sdq*.

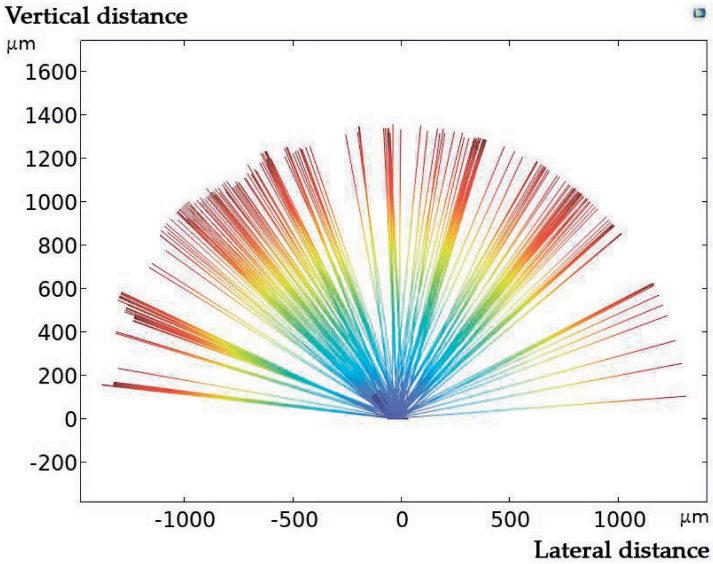


Figure 18. Reflectance diagram from a surface with a high value of local gradients *Sdq*.

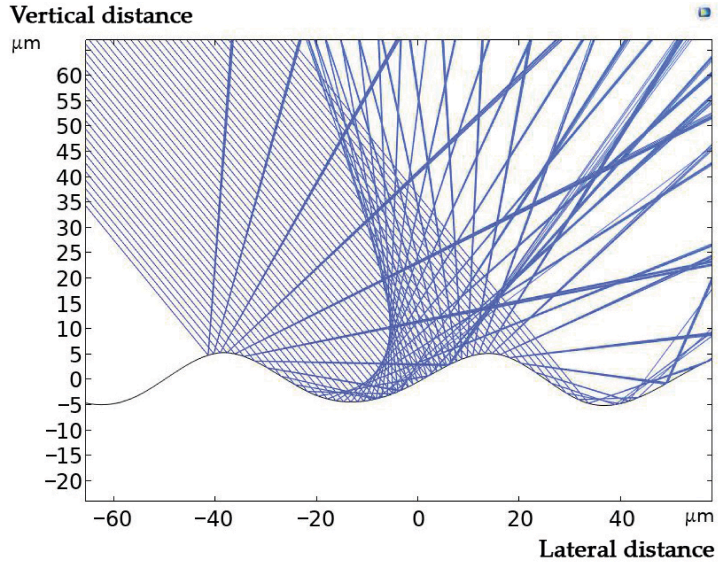


Figure 19. Light beam propagation diagram in a microstructure with a low value of local gradients *Sdq*.

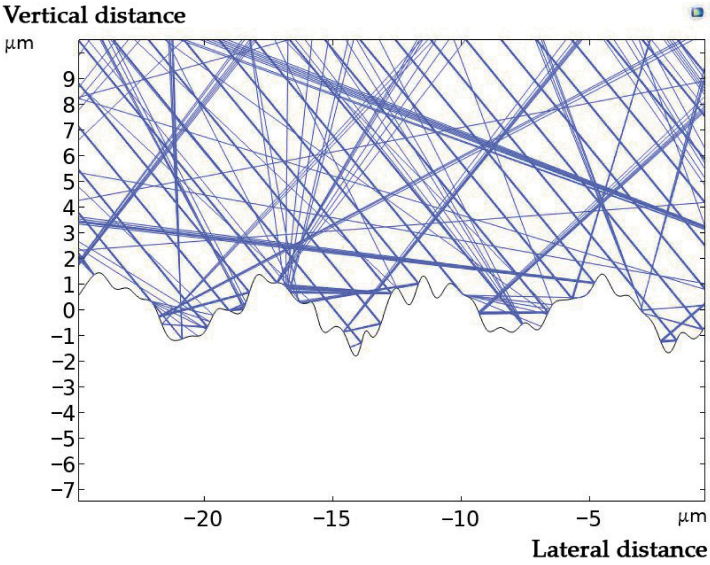


Figure 20. Light beam propagation diagram in a microstructure with a high value of local gradients *Sdq*.

4. Conclusions

Experimental investigations demonstrate that surface height distribution metrics play a pivotal role in evaluating the surface blackening achieved through femtosecond laser processing.

Based on visual assessments, it is concluded that the presence or absence of periodicity of the microstructures is not a decisive factor in determining the degree of blackening for AISI 321 steel.

A more relief microstructure, according to visual assessment, also contributes to surface blackening, despite the fact that, as noted earlier, a multiple increase in values does not lead to a corresponding increase in the degree of surface blackening, despite the fact that repeated processing increased the surface relief parameters by two times.

Additional post-processing of the surface without changing the processing mode does not lead to a twofold increase in the degree of surface blackening compared to the nature of the surface blackening obtained as a result of previous processing.

Repeated laser processing does not reduce the proportion of the surface that can be removed during subsequent running-in. Similarly, the proportion of depressions on the surface used to accumulate additives and lubricating coatings on the sample surface does

not change significantly. Thus, for a qualitative change in the sliding and optical properties of the surface, processing with modified laser parameters is necessary, rather than two-fold sequential processing in a fixed mode. It is demonstrated that secondary perpendicular processing in an identical regime is characterized by a micro-relief saturation effect. Although the root-mean-square roughness (*Sq*) and the developed interfacial area ratio (*Sdq*) continue to increase, the primary laser pass already establishes the highly absorbing structure. This renders repeated exposure energetically inefficient for any substantial improvement in optical performance. Consequently, this defines an optimization limit for simple pass duplication without altering the pulse parameters themselves.

The first stage of processing led to an increase in the value of the surface profile asymmetry parameter (*Ssk*), which observation signifies that the topographic peaks dominate the surface structure, over elements formed by depressions and cavities. This feature of the microrelief was preserved after repeated surface processing, but no noticeable increase in the value of the asymmetry parameter was noted.

At the first stage, the parameters such as the maximum peak height (*Sp*) increased the most, by 7.33 times, and the ten-point surface height (*S10z*) increased by 6.04 times. After repeated processing, the maximum relative increase in the maximum trench depth (*Sv*) parameter was noted, by 2.57 times, and the root-mean-square slope (*Sdq*) by 2.37 times.

Also, repeated processing did not qualitatively increase the surface blackness, which confirms the conclusion that an insignificant, within 5%, increase in the kurtosis value, characteristic of the surfaces under consideration, does not allow one to visually observe a significant contrast in blackness between these surfaces (Figure 2A,B).

It has been established that if the primary processing does not result in the formation of a periodic surface microstructure and a complex height distribution is not observed, then repeated surface processing in the same mode does not impart a periodic character to the surface structure and does not change the nature of the height distribution in accordance with the normal Gaussian distribution law.

A quantitative comparison of the topographical and optical data reveals a distinct correlation trend. Specifically, the 2.37-fold increase in the root mean square slope (*Sdq*) from 0.133 in the primary stage to 0.315 in the secondary stage aligns with the recorded reduction in average surface blackening from 16.6% to 14.4% ($p < 0.05$). This relationship is further supported by the ray optics simulations (Figures 13–20), which indicate that higher surface gradients, when coupled with a high kurtosis index (*Sku* > 17), promote more frequent multiple reflections and enhanced energy redistribution within the surface valleys. Thus, within the investigated processing range, the *Sdq* parameter serves as an indicator of light-trapping efficiency, bridging the gap between 3D-roughness evolution and the resulting optical response.

It was quantitatively established that secondary laser processing provides only a marginal improvement in optical blackening (up to 5%, from 16.6% to 14.4% in HSB brightness), despite a significant 2.37-fold increase in the surface slope parameter (*Sdq*). For industrial automation and marking applications, this indicates that the optical trap efficiency has reached an asymptotic limit. Therefore, for high-speed production lines, optimizing the primary laser fluence and scanning step is more resource-efficient and effective than implementing successive multi-pass strategies. This allows for achieving high-contrast markers with minimal processing time and energy consumption.

Author Contributions: Conceptualization, S.D. and B.A.A.; methodology, B.A.A., Y.B. and P.Z.; validation, S.D., B.A.A., Y.B. and M.K.; formal analysis, S.D.; investigation, S.D., Y.B., B.A.A., D.T., M.K., P.Z., M.L. and M.H.; resources, P.Z., S.D., Y.B., B.A.A., D.T. and M.L.; data curation, S.D., Y.B. and P.Z.; writing—original draft preparation, B.A.A., Y.B., D.T. and M.L.; writing—review and editing, P.Z., M.K. and S.D.; supervision, S.D.; project administration, M.H. All authors have read and agreed to the published version of the manuscript.

Funding: The general approach has been partially developed within the research projects supported by the National Research Foundation of Ukraine: "Formation and transformation of periodic nanocarbon-containing structures on metal surfaces with short-pulse laser, microwave, and plasma methods" (St. Reg. № 0124U000481, 2024–2026 years), and "Creation of experimental samples of rolling bearings with enhanced performance characteristics based on energy efficiency and durability criteria" (St. Reg. № 0125U001616, 2025–2026 years). This publication was created within the project Research of advanced technologies for increasing the efficiency of multivalent energy systems for sustainable industrial development, ITMS21 + code: 401101C504, co-funded by the European Union under the Programme Slovakia. This work was funded by the Slovak Research and Development Agency under contract No. APVV-21-0228 and No. VV-MVP-24-0190.

Data Availability Statement: The original contributions presented in this study are included in the article. Further inquiries can be directed to the corresponding author.

Conflicts of Interest: The authors declare no conflicts of interest. The funders had no role in the design of the study; in the collection, analyses, or interpretation of the data; in the writing of the manuscript; or in the decision to publish the results.

References

1. Plankovskyy, S.; Shypul, O.; Tsegelnyk, Y.; Brega, D.; Tryfonov, O.; Malashenko, V. Basic Principles for Thermoplastic Parts Finishing with Impulse Thermal Energy Method. In *Handbook of Research on Advancements in the Processing, Characterization, and Application of Lightweight Materials*; IGI Global: Hershey, PA, USA, 2022; pp. 49–87.
2. Khadka, N.; Yang, Y.; Hoffman, A.; Rosenberger, M.; Kinzel, E.C. Spectral Selectivity and Blackening through Direct-Write Femtosecond Micromachining. In *Proceedings of the High-Power Laser Materials Processing: Applications, Diagnostics, and Systems XIII*; Kleine, K.R., Kaierle, S., Eds.; SPIE: Bellingham, WA, USA, 2024; p. 20.
3. Xu, S.; Tan, L.; Yao, C.; Miao, X.; Lü, H.; Jiang, X.; Yuan, X. Anti-Reflective and Wetting Properties of Femtosecond Pulsed Laser Textured Al Alloy Surfaces. *Optik* **2021**, *242*, 167293. [CrossRef]
4. Hruška, P.; More-Chevalier, J.; Novotný, M.; Čížek, J.; Melikhova, O.; Fekete, L.; Poupon, M.; Bulíř, J.; Volfová, L.; Butterling, M.; et al. Effect of Roughness and Nanoporosity on Optical Properties of Black and Reflective Al Films Prepared by Magnetron Sputtering. *J. Alloys Compd.* **2021**, *872*, 159744. [CrossRef]
5. Yang, L.; Deng, Z.; He, B.; Özel, T. An Experimental Investigation on Laser Surface Texturing of AISI D2 Tool Steel Using Nanosecond Fiber Laser. *Lasers Manuf. Mater. Process.* **2021**, *8*, 140–156. [CrossRef]
6. Shimada, H.; Kato, S.; Watanabe, T.; Yamaguchi, M. Direct Laser Processing of Two-Scale Periodic Structures for Superhydrophobic Surfaces Using a Nanosecond Pulsed Laser. *Lasers Manuf. Mater. Process.* **2020**, *7*, 496–512. [CrossRef]
7. Florian, C.; Kirner, S.V.; Krüger, J.; Bonse, J. Surface Functionalization by Laser-Induced Periodic Surface Structures. *J. Laser Appl.* **2020**, *32*, 022063. [CrossRef]
8. Ding, K.; Wang, C.; Ding, Y.; Cao, P.; Li, S.; Zhang, X.; Lin, N.; Duan, J. Broadband Optical Absorption Copper Surface Fabricated by Femtosecond Laser for Sensitivity Enhancement of Thermoelectric Photodetector. *Opt. Laser Technol.* **2024**, *168*, 109942. [CrossRef]
9. Mamykin, S.V.; Gnilitskyi, I.M.; Dusheyko, M.G.; DeVol, T.A.; Bliznyuk, V.N. Femtosecond Laser Nano-Structuring for Surface Plasmon Resonance-Based Detection of Uranium. *Appl. Surf. Sci.* **2022**, *576*, 151831. [CrossRef]
10. Liu, C.; Zhuang, Z.; Chen, J.; Yip, W.S.; To, S. Atomic-scale investigation of Pt composition on deformation mechanism of AuPt alloy during nano-scratching process. *Surf. Interfaces* **2023**, *40*, 103126. [CrossRef]
11. Sheng, X.; Zhu, Z.; Liu, C. A Review of the Machining Mechanisms in Field-Assisted Cutting of Brittle Materials. *Micromachines* **2026**, *17*, 361. [CrossRef]
12. Xie, J.; Qiao, M.; Zhu, D.; Yan, J.; Deng, S.; He, G.; Luo, M.; Zhao, Y. Laser Induced Coffee-Ring Structure through Solid-Liquid Transition for Color Printing. *Small* **2023**, *19*, 2205696. [CrossRef]
13. Fang, F.; Lai, M.; Wang, J.; Luo, X.; Yan, J.; Yan, Y. Nanometric cutting: Mechanisms, practices and future perspectives. *Int. J. Mach. Tools Manuf.* **2022**, *178*, 103905. [CrossRef]
14. Zhuang, Z.; Du, H.; Yip, W.S.; Yin, T.; Zhao, Z.; Zhu, Z.; To, S. Development of a high-performance cutting device based on hybrid actuation for ultra-precision machining. *Mater. Des.* **2022**, *225*, 111420. [CrossRef]
15. *DIN EN ISO 25178-2:2023-09*; Geometrical Product Specifications (GPS)—Surface Texture: Areal—Part 2: Terms, Definitions and Surface Texture Parameters (ISO 25178-2:2021). ISO: Geneva, Switzerland, 2023.
16. Janos Richter, L.; Beckmann, C.M.; Ihlemann, J. UV Laser Generated Micro Structured Black Surface on Commercial TiO_2-Containing Glass. *Appl. Surf. Sci.* **2022**, *601*, 154231. [CrossRef]
17. Li, X.; Li, M.; Liu, H. Effective Strategy to Achieve a Metal Surface with Ultralow Reflectivity by Femtosecond Laser Fabrication. *Chin. Opt. Lett.* **2021**, *19*, 051401. [CrossRef]

18. Ruzova, T.A.; Haddadi, B. Surface Roughness and Its Measurement Methods—Analytical Review. *Results Surf. Interfaces* **2025**, *19*, 100441. [CrossRef]
19. Gadelmawla, E.S.; Koura, M.M.; Maksoud, T.M.A.; Elewa, I.M.; Soliman, H.H. Roughness Parameters. *J. Mater. Process. Technol.* **2002**, *123*, 133–145. [CrossRef]
20. Sarkar, P.; Kumar, M.; Sidpara, A.M. Parametric Investigation of Wire-EDM Parameters for Micro Channel as a Foundation of High-Quality Micro Needle Array Fabrication. *Proc. Inst. Mech. Eng. C J. Mech. Eng. Sci.* **2024**, *238*, 9527–9546. [CrossRef]
21. Marinello, F.; Pezzuolo, A. Application of ISO 25178 Standard for Multiscale 3D Parametric Assessment of Surface Topographies. *IOP Conf. Ser. Earth Environ. Sci.* **2019**, *275*, 012011. [CrossRef]
22. Wurm, M.; Geckeler, R.D. A New Method and a Novel Facility for Ultra Precise 2D Topography Measurement of Large Optical Surfaces. In *Optical Metrology in Production Engineering*; Osten, W., Takeda, M., Eds.; SPIE: Bellingham, WA, USA, 2004; p. 401.
23. Song, J.; Vorburger, T. Topography Measurements and Applications. *Philos. Trans. R. Soc. A Math. Phys. Eng. Sci.* **2006**, *377*, 62801T.
24. Molnar, V.; Szabo, G. Designation of Minimum Measurement Area for the Evaluation of 3D Surface Texture. *J. Manuf. Process.* **2022**, *83*, 40–48. [CrossRef]
25. Eifler, M.; Hering, J.; von Freymann, G.; Seewig, J. Manufacturing of the ISO 25178-70 Material Measures with Direct Laser Writing: A Feasibility Study. *Surf. Topogr.* **2018**, *6*, 024010. [CrossRef]
26. Holzer, L.; Indutnyi, F.; Gasser, P.H.; Münch, B.; Wegmann, M. Three-dimensional Analysis of Porous $BaTiO_3$ Ceramics Using FIB Nanotomography. *J. Microsc.* **2004**, *216*, 84–95. [CrossRef]
27. Menezes, P.L.; Kishore; Kailas, S.V. Effect of Surface Roughness Parameters and Surface Texture on Friction and Transfer Layer Formation in Tin–Steel Tribo-System. *J. Mater. Process. Technol.* **2008**, *208*, 372–382. [CrossRef]
28. Vukelic, D.; Prica, M.; Ivanov, V.; Jovicic, G.; Budak, I.; Luzanin, O. Optimization of Surface Roughness Based on Turning Parameters and Insert Geometry. *Int. J. Simul. Model.* **2022**, *21*, 417–428. [CrossRef]
29. Myshkin, N.K.; Grigoriev, A.Y.; Chizhik, S.A.; Choi, K.Y.; Petrokovets, M.I. Surface Roughness and Texture Analysis in Microscale. *Wear* **2003**, *254*, 1001–1009. [CrossRef]
30. Qahtani, F.; Shrotriya, P. Study the Effect of Changing the Surface Roughness and the Laser Focus Distance to the Aluminum Appearance Using Picosecond Laser. *Procedia Manuf.* **2019**, *34*, 214–221. [CrossRef]
31. Kusyi, Y.; Ivanov, V.; Korniy, S.; Datsko, B.; Hatala, M. Non-Destructive Evaluation of Quality Parameters of Al-Si Workpieces after Milling. *Int. J. Adv. Manuf. Technol.* **2025**, 1–23. [CrossRef]
32. Pawlus, P.; Reizer, R.; Wieczorowski, M. Functional Importance of Surface Texture Parameters. *Materials* **2021**, *14*, 5326. [CrossRef]
33. Garcell, E.M.; Guo, C. Colorful Multifunctional Surfaces Produced by Femtosecond Laser Pulses. *Opt. Mater. Express* **2019**, *9*, 1033–1040. [CrossRef]
34. Przestacki, D.; Majchrowski, R.; Marciniak-Podsadna, L. Experimental Research of Surface Roughness and Surface Texture after Laser Cladding. *Appl. Surf. Sci.* **2016**, *388*, 420–423. [CrossRef]
35. Vukelic, D.; Milosevic, A.; Ivanov, V.; Kocovic, V.; Santosi, Z.; Sokac, M.; Simunovic, G. Modelling and Optimization of Dimensional Accuracy and Surface Roughness in Dry Turning of Inconel 625 Alloy. *Adv. Prod. Eng. Manag.* **2024**, *19*, 371–385. [CrossRef]
36. Bizi-bandoki, P.; Valette, S.; Audouard, E.; Benayoun, S. Effect of Stationary Femtosecond Laser Irradiation on Substructures' Formation on a Mold Stainless Steel Surface. *Appl. Surf. Sci.* **2013**, *270*, 197–204. [CrossRef]
37. Buividas, R.; Mikutis, M.; Kudrius, T.; Greičius, A.; Šlekys, G.; Juodkazis, S. Femtosecond Laser Processing—A New Enabling Technology. *Lith. J. Phys.* **2012**, *52*, 301–311. [CrossRef]
38. Sugioka, K. Progress in Ultrafast Laser Processing and Future Prospects. *Nanophotonics* **2017**, *6*, 393–413. [CrossRef]
39. Fraggelakis, F.; Tsibidis, G.D.; Stratakis, E. Ultrashort pulsed laser induced complex surface structures generated by tailoring the melt hydrodynamics. *Opto-Electron. Adv.* **2022**, *5*, 210052. [CrossRef]
40. Saprykina, E.; Dobrotvorskyi, S.; Aleksenko, B.; Trubín, D.; Moskal, M. Analysis of parameters of laser-induced periodic microstructures (LIPSS) on the surface of stainless steel using autocorrelation functions. *Cut. Tools Technol. Syst.* **2025**, *102*, 37–49. [CrossRef]
41. Bonse, J.; Kirner, S.V.; Krüger, J. Laser-Induced Periodic Surface Structures (LIPSS). In *Handbook of Laser Micro- and Nano-Engineering*; Springer: Cham, Switzerland, 2021; pp. 879–936. [CrossRef]
42. Gaidys, M.; Žemaitis, A.; Gečys, P.; Gedvilas, M. Efficient picosecond laser ablation of copper cylinders. *Appl. Surf. Sci.* **2019**, *483*, 962–966. [CrossRef]
43. Mannion, P.; Magee, J.; Coyne, E.; O'Connor, G.M. Ablation thresholds in ultrafast laser micromachining of common metals in air. *SPIE Proc.* **2003**, *4876*, 470. [CrossRef]
44. COMSOL. COMSOL User's Guide. Ray Optics Module. COMSOL©. 2022. Available online: https://doc.comsol.com/6.1/doc/com.comsol.help.roptics/RayOpticsModuleUsersGuide.pdf (accessed on 26 April 2026).

Disclaimer/Publisher's Note: The statements, opinions and data contained in all publications are solely those of the individual author(s) and contributor(s) and not of MDPI and/or the editor(s). MDPI and/or the editor(s) disclaim responsibility for any injury to people or property resulting from any ideas, methods, instructions or products referred to in the content.